



Thermal process monitoring and control for a near-net-shape Wire and Arc Additive Manufacturing

Daniel Baier¹ · Franz Wolf¹ · Tobias Weckenmann¹ · Maja Lehmann¹ · Michael F. Zaeh¹

Received: 24 January 2022 / Accepted: 16 May 2022 / Published online: 14 June 2022
© The Author(s) 2022

Abstract

Wire and Arc Additive Manufacturing (WAAM) is a promising technology for the fabrication of large metal parts. During the process, the wire electrode is melted continuously or in a pulsating mode and deposited layer-by-layer onto a substrate. Due to the recurring energy input into the part during WAAM, adequate thermal management is crucial. The temperature distribution, especially the interlayer temperature in the part, is determined by the parameter settings as well as by the dwell times and can be monitored. This paper presents the cause-effect relationships between the interlayer temperature and the dwell times to enable a suitable temperature management. Thermal imaging was implemented during the manufacturing process, allowing the analysis of different interlayer dwell times and their effect on the interlayer temperatures. In addition, the influence of the temperature management on the geometric quality characteristics of the part was investigated. It was observed that a constant interlayer dwell time led to geometric irregularities in the part height and width. Monitoring the interlayer temperature is crucial in WAAM in order to maintain a constant temperature level along multiple layers for meeting the requirements for the geometry of the part and enabling near-net-shape manufacturing.

Keywords Additive Manufacturing · WAAM · Process monitoring · Ti-6Al-4V · Thermal management

1 Introduction

Additive Manufacturing (AM) processes are becoming increasingly important as the product complexity rises and the need for flexibility in industrial applications grows. Laser powder bed processes are already well established in industrial applications, but are restricted by limited build volumes and high processing times [1]. A promising technology for the economical manufacturing of large parts with medium complexity is Wire and Arc Additive Manufacturing (WAAM) [2]. Potential applications range from load-bearing steel structures in the construction industry [3] to large structural parts in the aviation industry [4]. The latter, in particular, require lightweight metal structures, as they are made from aluminum or titanium alloys [4].

By definition, WAAM is assigned to the Directed Energy Deposition (DED) processes [5]. One DED process that

favors a low energy input and a stable process is the Cold Metal Transfer (CMT) process [2].

This process is characterized by a pulsating ignition of the arc with a retraction movement of the wire electrode during the process and is classified under the metal inert / active gas welding [6]. A part is formed layer by layer by the deposition of a weld bead.

WAAM is an alternative to conventional manufacturing methods and can be integrated into existing process chains [2, 4]. WAAM enables better Buy-to-Fly-ratios (BTF-ratio) and reduces the tool wear, resulting in cost savings [2]. This is essential for cost-intensive materials, such as titanium alloys [2]. A subsequent milling step ensures that the net-shape and the surface quality comply with the part requirements. Accordingly, an important usage case in industrial applications, and one of the major challenges of near-net-shape manufacturing [7], is ensuring geometric accuracy to achieve low BTF-ratios [7, 8].

The target geometry of the WAAM parts and their accuracy are determined by selecting the process parameters and the build-up strategy. Several authors identified the travel speed and the wire feed speed as the main parameters influencing the geometry of single bead walls [9–11]. The tool

✉ Daniel Baier
daniel.baier@iwb.tum.de

¹ Institute for Machine Tools and Industrial Management, Technical University of Munich (TUM), Boltzmannstrasse 15, 85748 Garching, Germany

path planning, meaning the build-up strategy, becomes an important mean for adjusting the geometry of more complex parts [7, 12, 13].

In addition to these process parameters, the dwell times also significantly influence the dimensional accuracy. The dwell time is described by the time between the end of the welding and the start of the welding between individual layers. During this time the part can cool down. The shorter the dwell times, the higher are the interlayer temperatures. This can lead to a heat accumulation, resulting in part deformation. A number of researchers have studied this phenomenon.

Yang et al. [14] investigated the effect of the dwell times on the temperature characteristics, the cooling rates, and the geometric accuracy during WAAM, which is based on gas metal arc welding of multilayer walls made of steel. They showed that the heat accumulation of the manufactured part increased in higher layers. This effect was less pronounced with longer dwell times. Short dwell times led to a decreasing geometric accuracy.

Rocha et al. [15] confirmed this correlation between the dwell time and the heat accumulation. An increasing surface temperature of wider stainless steel walls could be mitigated by applying longer dwell times. They also found that long dwell times significantly increase the manufacturing time for the whole part.

The effect of the dwell time on the deviation in wall width of multilayer carbon steel walls was described by Lehmann et al. [9]. Short dwell times caused slumping of the weld bead. An uneven wall width and, therefore, low geometrical accuracy was observed.

Gonzalez et al. [16] concluded that a heating up of the specimen in higher layers is the cause for decreasing layer heights.

Controlling the interlayer temperature is important in order to preserve the geometric accuracy and prevent heat accumulation.

Wu et al. [17] developed and tested an active interlayer cooling based on a gas-shielding unit for the thermal management during the gas tungsten arc welding process. They were able to control the microstructure, the mechanical properties, and the thermal distortion [18, 19]. High geometrical inaccuracies were observed for short interlayer dwell times.

Vazquez et al. [8] implemented an interlayer cooling by using a water-cooled baseplate during the CMT-based WAAM of Ti-6Al-4V. The authors observed geometrical inaccuracies for short interlayer dwell times without the active cooling. The cooling system allowed for a more uniform structure.

Kozamernik et al. [20] stated that it is beneficial to directly control the interlayer temperature for a stable layer height and an improved geometric accuracy using the steel alloy G3Si1. The measurement of this temperature can be performed using an infrared pyrometer. The process is

controlled by the dwell time depending on the measured temperature. The authors also applied forced cooling to enhance the productivity by reducing the dwell times.

It has been shown in literature that the heat accumulation is caused by excessive interlayer temperatures and that this heat accumulation can be controlled by the dwell time. Reproducible part geometries can be achieved by monitoring the interlayer temperatures and controlling them. The thermal process management (interlayer temperatures and cooling rates) affects not only the geometry, but also mechanical properties and metallurgical aspects (covered in [8, 9, 17, 18, 21]). These aspects are subject to ongoing research. The literature review covers the geometric aspect of thermal management. The thermal management during WAAM by CMT welding of Ti-6Al-4 V has not been sufficiently investigated.

In this work, the effect of the thermal management was investigated during the CMT-based WAAM process using Ti-6Al-4 V. The influence of the interlayer temperatures and the dwell times on the part geometry was analyzed. For this purpose, statistically designed experiments were carried out. This study aims to enable the manufacturing of near-net-shape (meaning true-to-form) parts in a reproducible manner by monitoring and controlling both variables.

2 Methodology

To analyze the temperatures and their influence on the part geometries, the first step was to determine the interaction between the dwell time and the interlayer temperature. Subsequently, both influences on the geometry were investigated.

The target variables are the quality characteristics of the geometric accuracies of the parts. These values are quality indicators and a symbol of the near-net-shape manufacturing of parts. Additionally, the effective length $l_{\text{wall,meas}}$, the width $w_{\text{wall,meas}}$, and the height $h_{\text{wall,meas}}$ of a part, the surface waviness $sw_{\text{wall,meas}}$ on the part sides and the elevation at the top of the part $he_{\text{wall,meas}}$ are investigated. The target variables represent the shape and the dimensional deviations of the part (see Figs. 1 and 2). These target variables were analyzed by different post-process analysis methods and are explained in the following.

2.1 Geometric dimensions

Considering a hybrid manufacturing chain, the effective $w_{\text{wall,meas}}$, the $h_{\text{wall,meas}}$, and the $l_{\text{wall,meas}}$ are described as the necessary achievable dimensions that remain after a subsequent machining process. This corresponds to the maximum measured values and results in the final net-shape. These definitions of the measured values ensure that a part is not a scrap part due to large geometric deviations.

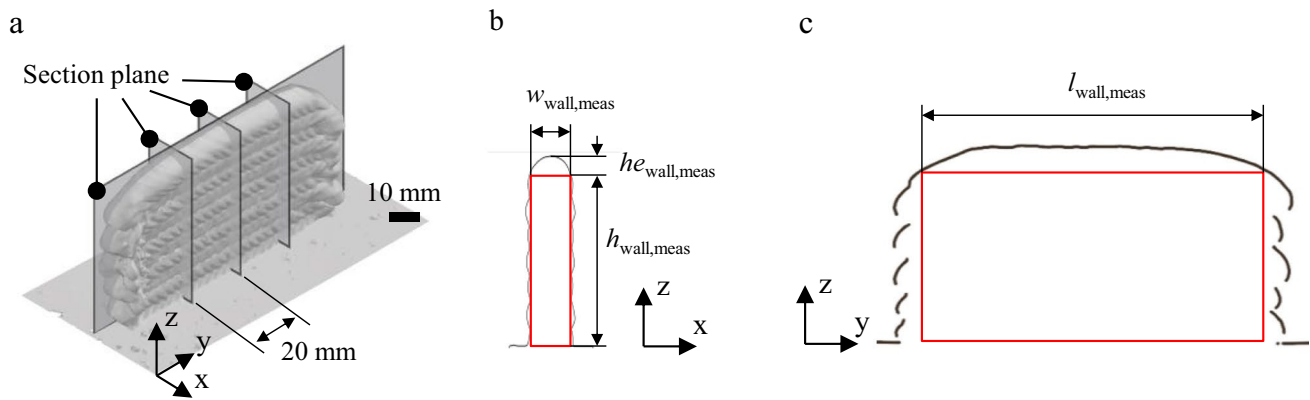


Fig. 1 Methodology for obtaining the part properties: **a** exemplary digitized part with the section planes, **b** the digitally cut specimen with the measured wall height, the width and the elevation at the top of the part and **c** the digitally cut part with the measured wall length

The built specimens were digitized in the post-process to obtain the target values. A Comet L3D 2 M light projector, a 3D scanner from Steinbichler was used (resolution of 1600×1200 pixels and a repeatability of $20 \mu\text{m}$). In 36° steps, the part was rotated around its z axis and images were recorded (see Fig. 1a). Point clouds were created on the surface of the part in each image using the COMET plus scanner software and then connected to form a triangle mesh. Each 3D model was exported as an STL file and analyzed with the computer-aided design software Fusion 360 by Autodesk.

Each value was determined on three cross-sections (section planes) evenly distributed on the specimen (see Fig. 1a). One cross-section was located at half of the length of the part. The two other sections were located at a distance of 20 mm from the center cross-section. The target values described below are the average values of the results of these three measuring points. To measure the width, a rectangle was drawn in each section plane. One line of the rectangle at the interface with the substrate was created at the bottom of the rectangle. Two perpendicular lines were added to form a tangent with the innermost point of the part contour. The position where the vertical lines contact the uppermost contour of the part was determined as the height. This rectangle was measured in width and height for all three sections as indicated in Fig. 1b. The same procedure was performed to measure the length of a part (see Fig. 1c). To evaluate the length of the part, a section plane was introduced in the build direction (see Fig. 1c). For this plane, the center section plane served as a reference. The center axis of the rectangle was determined from this cross-section. The specimen was digitally cut in x direction at this position. The length was then determined by a horizontal line drawn at the height position $h_{\text{wall, meas}}$ of the cross-section in

the center. The length measurement was obtained in a method similar to that used for the width. The length corresponds to the maximum distance between the innermost sides of the part (see Fig. 1c).

2.2 Geometric deviations

The $sw_{\text{wall, meas}}$ and the $he_{\text{wall, meas}}$ are defined as geometric deviations that negatively affect the geometric accuracy.

The measured elevation $he_{\text{wall, meas}}$ at the top of the part was established by drawing a horizontal tangent at the top of the wall (see Fig. 1b). The distance between the top of the rectangle and the tangent to the uppermost point of the part resulted in the value for the elevation of the part.

The surface waviness $sw_{\text{wall, meas}}$ on the sides of the parts was evaluated as a measure of the geometrical accuracy. According to DIN EN ISO 4287, the surface waviness describes the sections of a surface profile with a wavelength greater than the roughness profile. As the target geometry is likely to have an even and homogenous surface, the waviness profile must be machined.

Waviness profiles were obtained in the horizontal and the vertical direction (see Fig. 2) by using a structured light profilometer VR-3100 from Keyence. Values for the arithmetic mean of the surface profile w_a and the maximum height w_z (see DIN EN ISO 25175–2) were extracted. The target values were obtained as the mean value of eleven measurement lines in the horizontal direction and 21 measurement lines in the vertical direction (dimensions and spacing, see Fig. 2).

To distinguish the waviness from the roughness, a profile filter as defined in EN ISO 11562 with a cutoff wavelength of $\lambda_c = 0.8 \text{ mm}$ was applied to the surface profile.

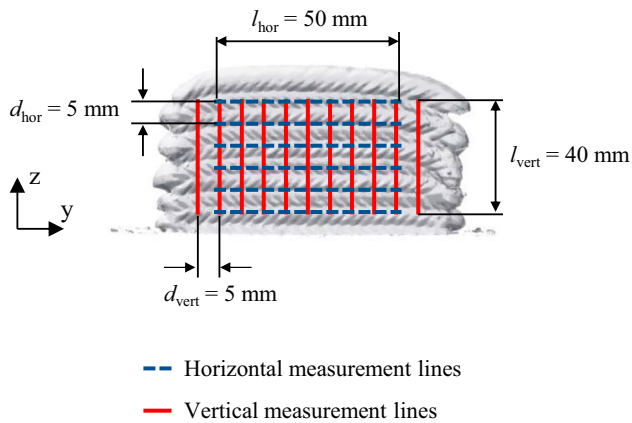


Fig. 2 Part with vertical and horizontal measuring lines for the surface waviness $sw_{\text{wall, meas}}$

2.3 Interlayer temperature and dwell time

In this paper, the interlayer temperature $T_{\text{Interlayer}}$ is defined as the temperature at the surface of the part prior to the welding of the subsequent layer. When the welding starts, the interlayer temperature corresponds to the temperature of the substrate plate, which is 24 °C in the present work. The dwell time t_{Dwell} can be set or measured as a welding parameter in the program code.

3 Experimental procedure

3.1 Materials, equipment, and measurement system

Figure 3 shows a drawing of the experimental set-up used in this study. A CMT welding power source, CMT Advanced 4000 R from Fronius International GmbH, was used for the experiments. The welding torch was moved over the substrate plate by an industrial 6-axis robot KR15/2 from Kuka AG.

The wire electrode (diameter of 1.2 mm) and substrate plate (thickness of 6 mm) were made from Ti-6Al-4V. The welding wire used was certified according to the standard AMS 4954. The substrate plate was certified according to the standard ASTM B265. The liquidus temperature of Ti-6Al-4V is 1650 °C ± 15 °C [22]. The thermal conductivity is temperature-dependent and increases at higher temperatures. While the conductivity of Ti-6Al-4V is 6.6 W/(m·K) at 20 °C, it increases to 17.5 W/(m·K) at 650 °C [22]. The mean coefficient of thermal expansion increases from $8.6 \cdot 10^{-6} \text{ K}^{-1}$ in the range of 20 °C to 100 °C to $9.7 \cdot 10^{-6} \text{ K}^{-1}$ between 20 and 650 °C [22].

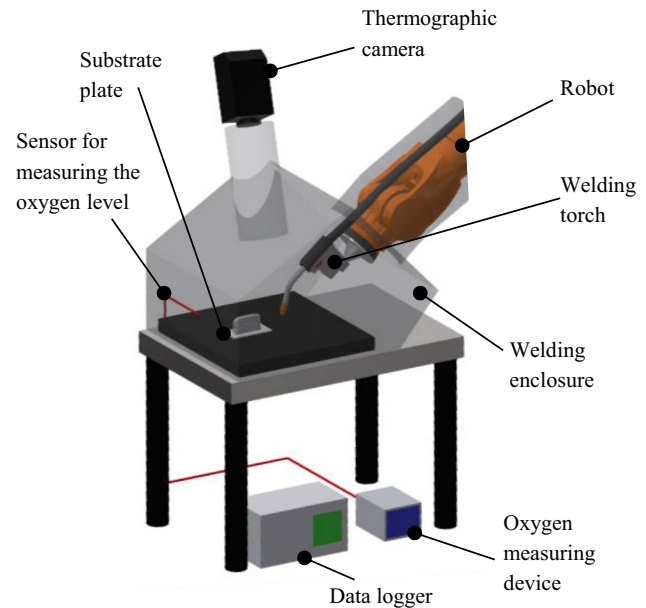


Fig. 3 Experimental set-up

Processing this material requires an inert gas atmosphere to protect the material from oxidation. For this, a special welding enclosure from Huntingdon Fusion Techniques HFT was used (see Fig. 3). This experimental set-up enabled the welding in an ambient atmosphere with less than 50 ppm of oxygen by using argon 4.6 as both forming and shielding gas.

As the interlayer temperature was evaluated during the experiments, the welding conditions (the temperature of the substrate plate and of the atmosphere) were kept constant during the process. To ensure that each manufactured specimen has a comparable and uniform initial condition at the start of the welding, both thermal welding conditions were kept below 50 °C. All welding conditions can be found in Appendix A.

The thermal monitoring and the oxygen measuring system components were installed to record the process data during the welding. The oxygen concentration in the process zone was measured using an oxygen measuring device, Oxygen Analyzer SGM7 from Zirox GmbH. The thermal welding conditions were characterized with type N thermocouples. A total of two thermocouples were used. To measure the substrate plate temperature, one thermocouple was placed centrally under the substrate plate of each wall. The other thermocouple was placed in the same position as the sensor for the oxygen measurement in the build chamber (see Fig. 3). These thermocouples were connected to a data logger ALMEMO from Ahlborn Mess- und Regelungstechnik GmbH. The interlayer temperature values were measured with a thermographic camera X6900sc from FLIR Systems GmbH.

3.2 Build-up strategy

The investigations focused on the manufacturing of multilayer walls. The parts were deposited with alternating bidirectional layers. This build-up strategy was combined with the oscillating motion and the edge rounding of the welding torch. A schematic representation of the robot path is shown in Fig. 4. The oscillating motion as a tool path enables the welding of wide walls. The variables defined as welding parameters for the weaving technique are shown in Fig. 4.

The weaving width a and the weaving length b were the movement of the welding torch in x and in y direction and were set at $a = 14$ mm and $b = 100$ mm. The weaving step d was the distance in y direction between the single oscillation movements in x direction and was set to $d = 4$ mm. The starting point of the curve e was the distance to the maximum oscillation point, where the curve motion started and was set to $e = 1$ mm. The displacement of the welding torch in z direction was set at $f = 6.1$ mm.

A CMT characteristic 1895 was used for the experiments as the welding program. This characteristic belongs to the short arc welding processes. In addition to the wire feed speed, the travel speed of the welding torch, the arc length correction factor, and the dynamic correction factor were kept constant. The travel speed of the welding torch was defined along the continuous robot path and means along the welding direction (see Fig. 4). The arc length correction factor affects the

deposition frequency of a single droplet and the duration of the arc ignition [11]. The dynamic correction factor influences the slope behavior of the current. Further details on the welding parameters held constant during the experiments are given in Appendix A.

3.3 Experimental plan (EP)

To describe the cause-effect relationships between the dwell times and the interlayer temperatures and to investigate their influence on the accuracy of the part, two different experimental studies were conducted. The welding parameters held constant during both experimental plans (EP) are described in Appendix A. Both statistically designed experiments were planned with full factorial designs with three steps and three executions each.

Varied interlayer dwell times applied in the first EP (EP1) and varied interlayer temperatures in the second EP (EP2) are described as variable welding parameters in Appendix A.

EP1 addressed the cause-effect relationship between the set interlayer dwell time t_{Dwell} and the resulting interlayer temperature $T_{Interlayer}$ as well as the final geometry of the built part. In this EP1, the measured dwell time was used as a trigger value t_{Dwell} for the start of the welding of the next layer. T_{Dwell} was set to 50 s, 400 s, and 750 s.

EP2 was performed to describe and quantify the correlation between $T_{Interlayer}$ and the resulting t_{Dwell} as well as the final geometry of the part. In this EP2, the measured interlayer temperature was used as a trigger temperature $T_{Interlayer}$ for the start of the welding of the next layer. $T_{Interlayer}$ was set to 50 °C, 300 °C, and 550 °C.

Due to the system limitations, higher interlayer temperatures are not considered as they would damage the machine components.

The measured target values, are $w_{wall,meas}$, $h_{wall,meas}$, $l_{wall,meas}$, $sw_{wall,meas}$, and, $he_{wall,meas}$, which were analyzed in both EPs.

4 Results and discussion

4.1 Analysis of the interlayer temperature and the dwell time

To understand the relationship between the interlayer temperature and the dwell time, one variable was measured at different layers while the other was held constant, and vice versa. In Fig. 5a, the interlayer temperature is shown for three different dwell times, and in Fig. 5b the dwell time is plotted for three different interlayer temperatures. In all

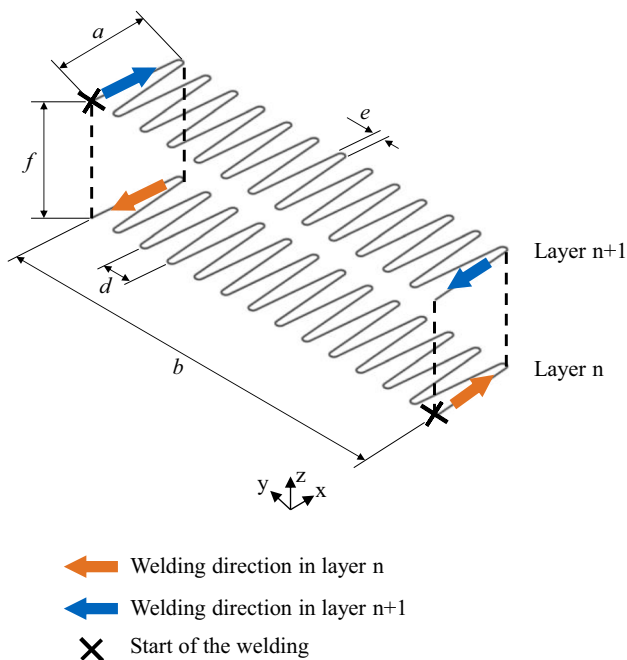


Fig. 4 Build-up strategy

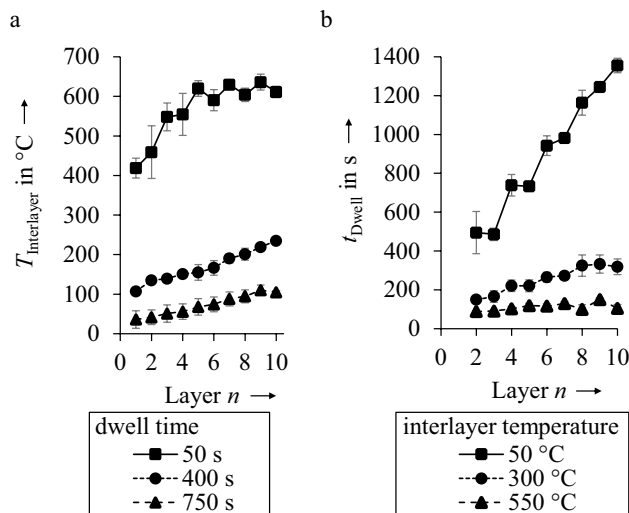


Fig. 5 **a** EP1: Measured interlayer temperature over the number of layers as a function of the constant set dwell time until the start of the welding; **b** EP2: measured dwell time until the start of the welding over the number of layers as a function of the constant set interlayer temperature

figures the error bars indicate the empirical standard deviation determined from the three repetitions of the executions.

For a dwell time of 50 s, the interlayer temperature rises from about 410 °C in the first layer to 600 °C in the fifth layer, forming a temperature gradient of 200 °C. From the sixth layer on, a constant temperature of 600 °C is established, which remains until the last layer.

The temperature gradient of the measured interlayer temperature curve decreases at dwell times of 400 s and 750 s. The temperature differences between the first and the last layers are not significant. For both dwell times, an approximately linear increase in the measured temperature values was observed.

At a controlled interlayer temperature in Fig. 5b of 50 °C, a large increase in the dwell time was measured in the higher layers. At an interlayer temperature of 300 °C, the dwell time in the higher layers rises only slightly. At 550 °C, the resulting dwell time shows a constant value of about 100 s between each layer.

Due to the low thermal conductivity of Ti-6Al-4V, the interlayer temperature increases significantly for a constant dwell time of 50 s, because the heat cannot dissipate away from the component fast enough. Only in the higher layers an equilibrium is reached at a high temperature. To keep a constant temperature of 50 °C in the component, the dwell time must be strongly adjusted.

Yang et al. [14] described the growing accumulation of the heat in the higher layers when using steel wire. This effect was also shown to be present using Ti-6Al-4V wire. A long dwell time is necessary to maintain low interlayer

temperatures, to achieve a constant temperature distribution, and to avoid heat accumulation. The control of the dwell time in each layer is therefore unavoidable to keep a constant interlayer temperature in every single layer. As Wu et al. [17] investigated, one option to proactively influence and reduce the dwell time is to add an active cooling system to the experimental set-up.

4.2 Analysis of the geometric dimensions

Figure 6 shows the results of the measurements of the total wall height and the total wall width for three different dwell times.

A long dwell time of 400 s and 750 s results in walls with a smaller width and a larger height compared to a dwell time of 50 s.

The effective width at a dwell time of 50 s is 12 mm which decreases to 11 mm for a 750 s dwell time. The effective height for a 50 s dwell time is 54.5 mm. At 400 s and 750 s, the height is approximately 58 mm.

The results for different interlayer temperatures are shown in Fig. 7, where the height and the width also correlate with the interlayer temperature.

At an interlayer temperature of 50 °C (this corresponds to a long dwell time, see Fig. 5), a height of about 58 mm is obtained. At 300 °C, the height is 56 mm, and at 550 °C, 54.5 mm. The convergence to a constant value observed in the EP1 (see Fig. 6) with long dwell times was not identified within the limited temperature range in the EP2.

An interlayer temperature of 50 °C resulted in walls with a width of about 10.7 mm, while at 550 °C a width of 11.7 mm was obtained.

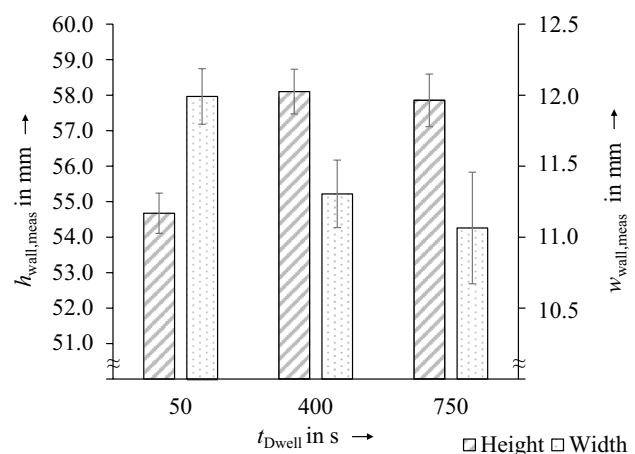


Fig. 6 EP1: Measured height and width of the wall against the constant set dwell time until the start of welding

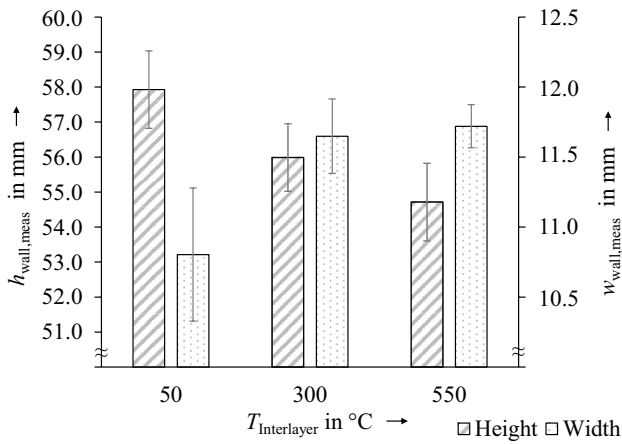


Fig. 7 EP2: Measured height and width of the wall over the constant interlayer temperature

In both studies, the standard deviation is greater with long dwell times or low interlayer temperatures. This shows that greater instabilities are present in the process in those parameter regimes than at higher interlayer temperatures and shorter dwell times. This can be explained by the higher temperature gradients at the start of the welding. The longer the dwell time is, the lower is the interlayer temperature and vice versa (see Fig. 5a and b). When welding on a layer that

has a proportionally low interlayer temperature, the temperature gradient increases due to the melting of the welding wire.

In conclusion, the total wall width tends to increase with higher interlayer temperatures (see Fig. 8a and b), while the total wall height decreases (see Fig. 8c and d). When welding a new layer, the interlayer temperature represents the temperature of the previous layer. Consequently, high interlayer temperatures lead to a lower temperature gradient between the melt pool and the previous layer. Due to this lower temperature gradient, a heat accumulation occurs. Although the thermal conductivity is increased at higher temperatures (see Sect. 3.1), this is not sufficient for enough heat dissipation. Therefore, the temperatures remain above the melting point of Ti-6Al-4V for a longer time. Combined with the gravitational and the surface tension forces, this leads to an increased flattening of the melt pool. This results in decreased heights and increased widths of single layers, which leads to a lower overall height and a larger overall width of the part. While this effect was studied and analytically described in the literature for single-bead walls [23], the presented results indicate that it can be transferred to wider walls manufactured by using a weaving technique.

The influence of the interlayer temperature and the dwell time on the height must be considered in the path planning. As Kozamernik et al. [20] found in their investigation using a steel wire, a monitoring of the interlayer temperature is beneficial for maintaining a stable layer height. For a near-net-shape production and to reach the target height at higher interlayer temperatures, more layers must be built. It can also be seen from the width measurement results that the targeted width of 14 mm (see Appendix A) was not achieved for any of the parts. Consequently, an addition to the width

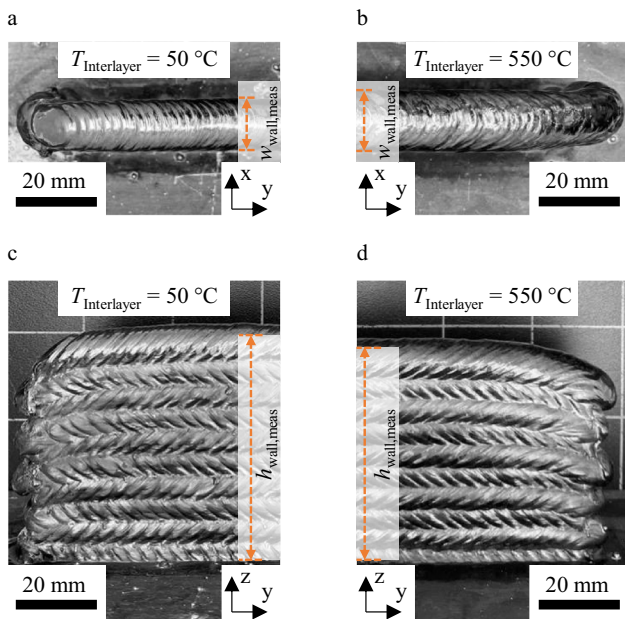


Fig. 8 EP2: Pictures of built walls measured by the methodology described in Sect. 2.1 to visualize the width at $T_{\text{Interlayer}} = 50\text{ °C}$ **a** and $T_{\text{Interlayer}} = 550\text{ °C}$ **b**; EP2: pictures of built walls measured by the methodology described in Sect. 2.1 to visualize the height and length at $T_{\text{Interlayer}} = 50\text{ °C}$ **c** and $T_{\text{Interlayer}} = 550\text{ °C}$ **d**

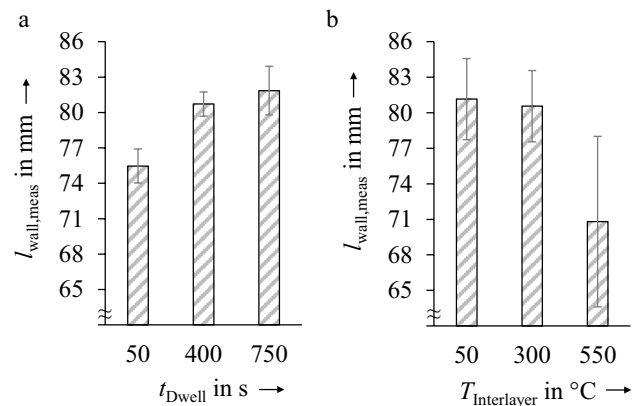


Fig. 9 **a** EP1: Measured length of the wall against the constant set dwell time; **b** EP2: measured length of the wall against the constant set interlayer temperature

depending on the interlayer temperature must also be specified in the process planning.

Figure 9a shows the influence of the set dwell time on the wall length. In Fig. 9b, the length is plotted against the interlayer temperature.

A dwell time of 50 s results in shorter effective lengths compared to longer dwell times. At a dwell time of 50 s, an effective length of 75 mm occurs. At dwell times of 400 s and 750 s, the effective lengths are about 81 mm and 82 mm. The same length can be reached at the interlayer temperatures of 50 °C and 300 °C. At an interlayer temperature of 550 °C, a length of 70 mm was obtained. However, this length has a high standard deviation. This indicates that greater instabilities exist in the process at 550 °C than at lower interlayer temperatures.

The effective length is mainly determined by decreasing layer heights towards both ends of the wall (see Fig. 1c). These occur due to molten metal flowing down at the ends of the wall, causing an additional rounding (see Fig. 8c and d). As described above, higher interlayer temperatures cause increased flattening at the ends of the wall. This is assumed to cause the decrease of the effective lengths for high interlayer temperatures and short dwell times.

The 100 mm length initially set (see Appendix A) in the build-up strategy was not achieved. Consequently, more material must be applied to the ends of a wall.

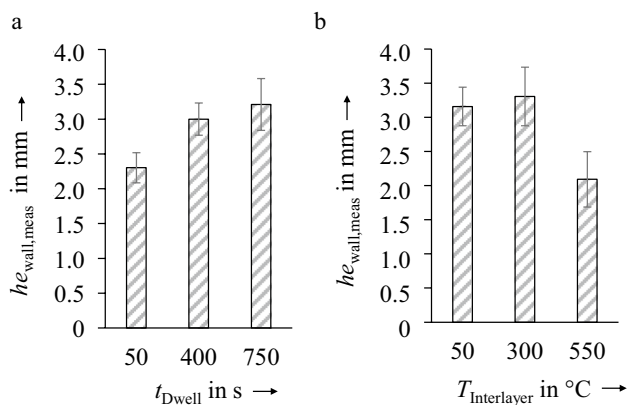


Fig. 10 a EP1: Measured elevation at the top of the wall against the constant set dwell time before the start of the welding; b EP2: measured elevation at the top of the wall against the constant set interlayer temperature

4.3 Analysis of the geometric deviations

Figure 10 shows the dependence of the elevation at the top of the part on the three different dwell times (Fig. 10a) and on the interlayer temperatures (Fig. 10b).

The elevation increases for the dwell times 400 s and 750 s when compared to the dwell time 50 s (see Fig. 10a). At 50 s, an elevation $he_{wall,meas}$ at the top of the part equal to 2.3 mm was measured (see Fig. 11a). This increases to 3.0 mm for 400 s. At 750 s, 3.1 mm elevation resulted (see Fig. 11b).

Figure 10b depicts a drop in the elevation to 2.0 mm at an interlayer temperature of 550 °C. The elevations at the top of the part at 50 °C and 300 °C have similar values of 3.1 mm and 3.2 mm respectively.

This quantity is mainly influenced by the conditions while welding the last layer. The effect of higher interlayer temperatures resulting in larger and flatter melt pools due to a lowered heat dissipation (described in Sect. 4.2) also applies in the last deposited layer. A flatter last layer geometry that would be expected for higher interlayer temperatures is represented by a lower top elevation $he_{wall,meas}$. The results for a dwell time of 50 s in EP1 and an interlayer temperature of 550 °C in EP2 support this assumption. There was no significant effect on $he_{wall,meas}$ observed between the dwell times of 400 s and 750 s in EP1 and between the interlayer temperatures of 50 °C and 300 °C in EP2. In contrast to the results in Sect. 4.2, it is assumed that the influence is too weak to be measured for dwell times from 400 s to 750 s and interlayer temperatures of 50 °C to 300 °C.

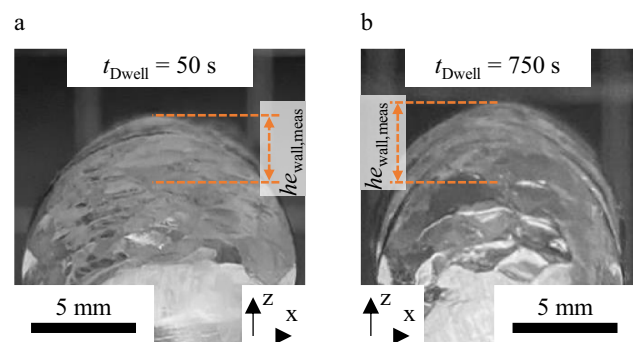


Fig. 11 EP1: Pictures of the last layers of built walls measured by the methodology described in Sect. 2.2 to visualize the elevation at the top at $t_{Dwell} = 50$ s a and $t_{Dwell} = 750$ s b

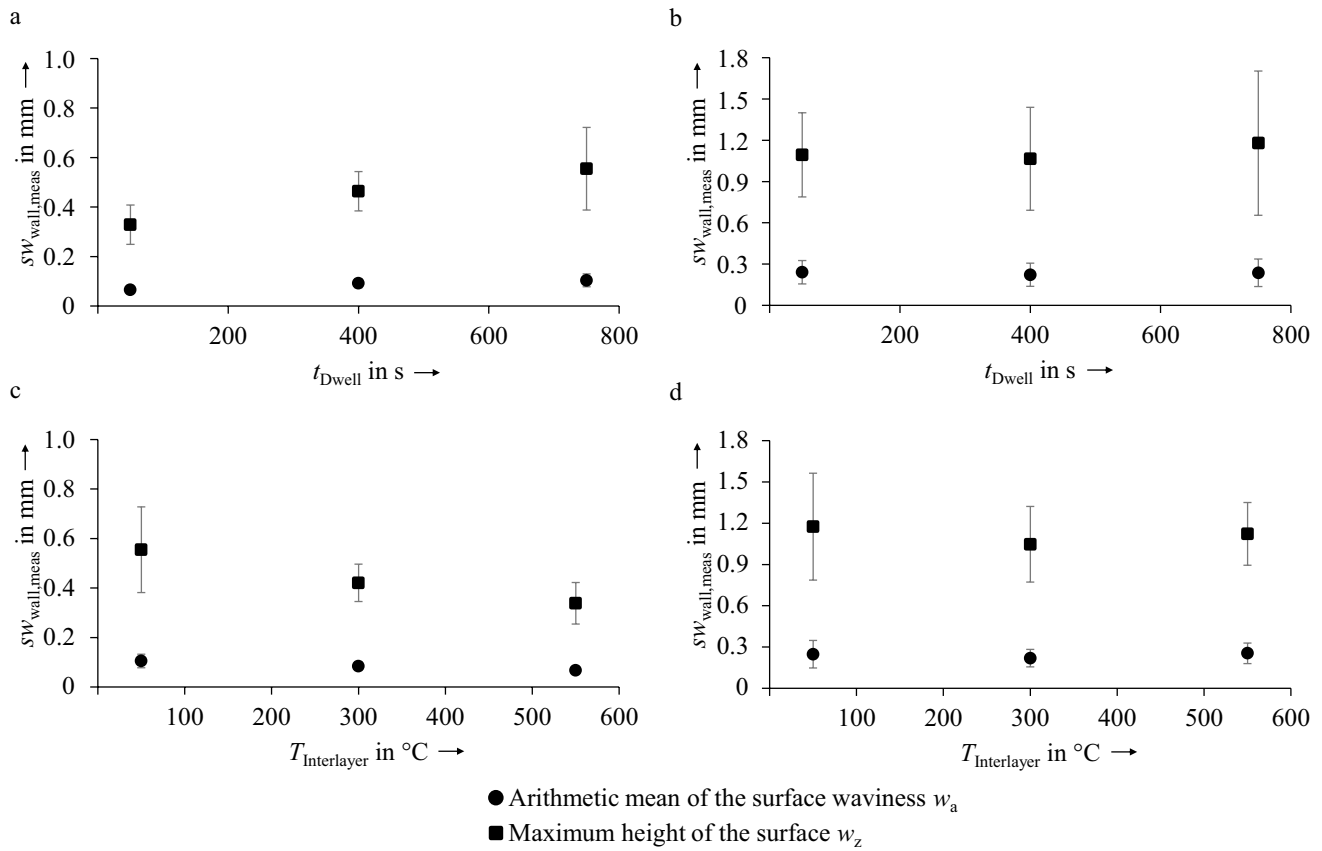


Fig. 12 EP1: The measured surface waviness in the horizontal **a** and the vertical **b** direction of the wall plotted against the constant set dwell time until the start of the welding; EP2: the measured surface

waviness in the horizontal **c** and the vertical **d** direction of the wall plotted against the constant set interlayer temperature

The elevation represents a geometrical deviation that must be removed in the subsequent machining process. A large elevation at the top of the part is detrimental to the process stability. It represents a rounding of the surface, which is unfavorable for the deposition welding process of the subsequent layer. The uneven distance between the wire electrode and the part (stick-out), as well as the sliding of the wire electrode on the edge of the part when the arc is reignited, led to an unstable WAAM process in the higher layers and resulted in unfavorable spatter during the study.

Figure 12a shows the results of the evaluation of the lateral surface waviness $SW_{wall,meas}$ against the dwell time in the horizontal direction of the measurement (as depicted in Fig. 2). The data points for the arithmetic mean of the surface waviness w_a and the maximum profile depth w_z are included. The same data points in the vertical direction are shown in Fig. 12b (as depicted in Fig. 2).

In Fig. 12a and b, w_a remains constant in the vertical and in the horizontal direction without an influence of the dwell time at approximately 0.1 mm (in Fig. 12a) and 0.2 mm (in Fig. 12b). In the horizontal measurement direction, an increase in w_z was observed with an increasing dwell time.

With an increase in the dwell time from 50 s to 400 s, w_z increases slightly from 0.3 mm to 0.4 mm. A slight trend towards higher values for the maximum profile depth at long dwell times can be identified (to $w_z=0.6$ mm at 750 s dwell time). In contrast, no influence of the dwell time on the vertical measurement points could be detected. The scatter of values tends to be greater for long dwell times.

Figure 12c shows the influence of the interlayer temperature on the waviness in the horizontal direction and Fig. 12d in the vertical direction.

The arithmetic mean is constant in both measuring directions and no influence of the interlayer temperature can be detected. In the horizontal direction, w_a remains equal to 0.1 mm at all temperature levels. In the vertical direction, w_a remains equal to 0.2 mm.

At higher interlayer temperatures, the waviness w_z decreases uniformly and constantly in the horizontal measuring direction from 0.6 mm to 0.3 mm. No significant influence of the temperature was observed in the vertical measuring direction. Low interlayer temperatures have a higher standard deviation for w_z .

The vertical surface waviness is influenced by how the deposited layers fuse together. The horizontal surface waviness mainly depends on the fusing between consecutive weaving steps (see Fig. 4). Based on this consideration, it may be assumed that the dwell time and the interlayer temperature influence the surface waviness via their influence on the melt pool geometry (described in Sect. 4.1). The presented results show that neither the dwell time nor the interlayer temperature have a significant influence. It is assumed that the bilateral alternating build-up strategy (see Fig. 4) allows the part to be heated adequately uniformly. As a result, all layers are heated evenly, resulting in a uniform waviness along the part.

An increased surface waviness would have to be considered in the path planning, since the waviness must be machined after the WAAM process to achieve flat side surfaces [4].

5 Conclusions and outlook

In WAAM, weld beads are deposited in layers on top of each other to create a three-dimensional part. The choice of process parameters influences the temperature balance of the part. This temperature balance influences the geometric quality characteristics of the part. Therefore, appropriate heat management during the WAAM process is very important.

This paper presents the influence of the interlayer temperature on the geometrical properties of Ti-6Al-4V parts. The interlayer temperature has a significant influence on the geometry of walls. The effects of the different interlayer temperatures and the dwell times on the behavior of the effective

wall width, the height, and the length, as well as on the elevation at the top of the part and the surface waviness were experimentally investigated.

The key findings of this paper are summarized below:

- For the manufacturing of a reproducible wall geometry, the interlayer temperature must be monitored and controlled when using a CMT-based WAAM process and Ti-6Al-4V.
- With a small part size, long dwell times are required in order to have low interlayer temperatures.
- In the first layers, the low temperature of the substrate plate at $< 50\text{ }^{\circ}\text{C}$ means that a high interlayer temperature of $550\text{ }^{\circ}\text{C}$ cannot be maintained.
- Due to the low thermal conductivity of Ti-6Al-4V, it was shown that the thermal equilibrium can only be achieved in the higher layers using short dwell times or high interlayer temperatures.
- The height can be influenced more by a controlled interlayer temperature than by a controlled dwell time.
- An interlayer temperature of $300\text{ }^{\circ}\text{C}$ is preferable for manufacturing components with higher stability, rather than $50\text{ }^{\circ}\text{C}$ and $550\text{ }^{\circ}\text{C}$, to avoid instabilities in height, width, and length.
- Different interlayer temperatures and dwell times have no significant effect on the surface waviness of the walls.

In this context, future research activities will include automatic signal interpretation. The online quality assurance is intended to facilitate the machine operation and to identify the potential geometric accuracies of the parts at an early stage. Further work will deal with the technological assessment of the WAAM process. The influence of the process parameters on the microstructure will also be part of further investigations.

Appendix A: Overview of input parameters

Category Norm	Category	Symbol	Value	Description
Welding parameters	Constant welding parameters	k_l	- 14 %	Arc length correction factor
		k_d	3.7	Dynamic control factor
		Q_{gTorch}	7 l/min	Volume flow of the shielding gas through the welding torch
		$Q_{gEnclosure}$	35 l/min	Volume flow of the shielding gas into the welding enclosure
		Δ	90°	Angle of the contact tip to the substrate plate
		s	15 mm	Distance of the contact tip to the substrate plate
		t_{GPre}	0.5 s	Time, the gas streams through the torch before the arc ignition.
		t_{GPost}	0.5 s	Time, the gas streams trough the welding torch after the welding process.
		v_{WFS}	8 m/min	Wire feed speed of the electrode
	v_{TS}	800 mm/min	Travel speed of the welding torch	
	Variable welding parameters	EP1: T_{Dwell}	50 s 400 s 750 s	Interlayer dwell time
		EP2: $T_{Interlayer}$	50 °C 300 °C 550 °C	Interlayer temperature
	Welding conditions	$O_2 Start$	≤ 50 ppm	Oxygen concentration at the start of the welding
$T_{Substrate}$		≤ 50 °C	Temperature underneath the substrate at the start of welding	
$T_{Enclosure}$		≤ 50 °C	Maximum temperature in the welding enclosure at the weld start	

Acknowledgements We hereby express our gratitude to the German Federal Ministry of Economic Affairs and Climate Action for its funding of the research activities. Some of the findings in this paper were achieved within the scope of the research project “REGULUS” (grant reference 20W1709D).

Funding Open Access funding enabled and organized by Projekt DEAL.

Open Access This article is licensed under a Creative Commons Attribution 4.0 International License, which permits use, sharing, adaptation, distribution and reproduction in any medium or format, as long as you give appropriate credit to the original author(s) and the source, provide a link to the Creative Commons licence, and indicate if changes were made. The images or other third party material in this article are included in the article's Creative Commons licence, unless indicated otherwise in a credit line to the material. If material is not included in the article's Creative Commons licence and your intended use is not permitted by statutory regulation or exceeds the permitted use, you will need to obtain permission directly from the copyright holder. To view a copy of this licence, visit <http://creativecommons.org/licenses/by/4.0/>.

References

- Williams S, Martina F, Wood D, Garcia Colomo A (2020) A comparison framework to support the selection of the best additive manufacturing process for specific aerospace applications. IJRAPIDM 9:1. <https://doi.org/10.1504/IJRAPIDM.2020.10019230>
- Williams SW, Martina F, Addison AC, Ding J, Pardal G, Colegrove P (2016) Wire + Arc Additive Manufacturing. Mater Sci

- Technol 32:641–647. <https://doi.org/10.1179/1743284715Y.0000000073>
- Weger D, Baier D, Straßer A, Pröttung S, Kränkel T, Bachmann A, Gehlen C, Zaeh M F (2020) Reinforced particle-bed printing by combination of the selective paste intrusion method with Wire and Arc Additive Manufacturing—a first feasibility study. Second RILEM international conference on concrete and digital fabrication, vol 28. Springer International Publishing, Cham, pp 978–987. https://doi.org/10.1007/978-3-030-49916-7_95
- Fuchs C, Baier D, Elitzer D, Kleinwort R, Bachmann A, Zaeh MF (2019) Additive manufacturing for structural components in aerospace engineering. ZWF Zeitschrift für wirtschaftlichen Fabrikbetrieb 114:431–434. <https://doi.org/10.3139/104.112124>
- DIN Deutsches Institut fuer Normung e. V. (2018) Additive manufacturing—general principles—terminology (ISO/ASTM DIS 52900). preprint
- Bruckner J (2013) Schweißpraxis aktuell: CMT-Technologie: Cold Metal Transfer—ein neuer Metall-Schutzgas-Schweißprozess. WEKA-Media, Kissing, Germany
- Ding J, Martina F, Williams S (2015) Production of large metallic components by additive manufacture—issues and achievements
- Vázquez L, Rodríguez N, Rodríguez I, Alberdi E, Álvarez P (2020) Influence of interpass cooling conditions on microstructure and tensile properties of Ti-6Al-4V parts manufactured by WAAM. Weld World 64:1377–1388. <https://doi.org/10.1007/s40194-020-00921-3>
- Lehmann T, Jain A, Jain Y, Stainer H, Wolfe T, Henein H, Qureshi AJ (2020) Concurrent geometry- and material-based process identification and optimization for robotic CMT-based wire arc additive manufacturing. Mater Des 194:108841. <https://doi.org/10.1016/j.matdes.2020.108841>
- Ding D, Pan Z, Cuiuri D, Li H (2015) Wire-feed additive manufacturing of metal components: technologies, developments and future interests. Int J Adv Manuf Technol 81:465–481. <https://doi.org/10.1007/s00170-015-7077-3>
- Baier D, Bachmann A, Zaeh MF (2020) Towards wire and Arc Additive Manufacturing of high-quality parts. Procedia CIRP 95:54–59. <https://doi.org/10.1016/j.procir.2020.01.180>

12. Lockett H, Ding J, Williams S, Martina F (2017) Design for Wire + Arc Additive Manufacture: design rules and build orientation selection. *J Eng Des* 28:568–598. <https://doi.org/10.1080/09544828.2017.1365826>
13. Wang X, Wang A, Li Y (2019) A sequential path-planning methodology for Wire And Arc Additive Manufacturing based on a water-pouring rule. *Int J Adv Manuf Technol* 103:3813–3830. <https://doi.org/10.1007/s00170-019-03706-1>
14. Yang D, Wang G, Zhang G (2017) Thermal analysis for single-pass multilayer GMAW based additive manufacturing using infrared thermography. *J Mater Process Technol* 244:215–224. <https://doi.org/10.1016/j.jmatprotec.2017.01.024>
15. Silva R H G e, Rocha P C J, Rodrigues M B, Pereira M, Galeazzi D (2020) Analysis of Interlayer Idle Time as a Temperature Control Technique in Additive Manufacturing of Thick Walls by Means of CMT and CMT Pulse Welding Processes. *Soldag insp* 25. <https://doi.org/10.1590/0104-9224/si25.01>
16. González J, Rodríguez I, Prado-Cerqueira J-L, Diéguez JL, Pereira A (2017) Additive manufacturing with GMAW welding and CMT technology. *Proc Manuf* 13:840–847. <https://doi.org/10.1016/j.promfg.2017.09.189>
17. Wu B, Ding D, Pan Z, Cuiuri D, Li H, Han J, Fei Z (2017) Effects of heat accumulation on the arc characteristics and metal transfer behavior in Wire Arc Additive Manufacturing of Ti6Al4V. *J Mater Process Technol* 250:304–312. <https://doi.org/10.1016/j.jmatprotec.2017.07.037>
18. Wu B, Pan Z, Ding D, Cuiuri D, Li H, Fei Z (2018) The effects of forced interpass cooling on the material properties of wire arc additively manufactured Ti6Al4V alloy. *J Mater Process Technol* 258:97–105. <https://doi.org/10.1016/j.jmatprotec.2018.03.024>
19. Ding D, Wu B, Pan Z, Qiu Z, Li H (2020) Wire arc additive manufacturing of Ti6Al4V using active interpass cooling. *Mater Manuf Processes* 35:845–851. <https://doi.org/10.1080/10426914.2020.1732414>
20. Kozamernik N, Bračun D, Klobčar D (2020) WAAM system with interpass temperature control and forced cooling for near-net-shape printing of small metal components. *Int J Adv Manuf Technol* 110:1955–1968. <https://doi.org/10.1007/s00170-020-05958-8>
21. Wu B, Pan Z, Ding D, Cuiuri D, Li H (2018) Effects of heat accumulation on microstructure and mechanical properties of Ti6Al4V alloy deposited by wire arc additive manufacturing. *Addit Manuf* 23:151–160. <https://doi.org/10.1016/j.addma.2018.08.004>
22. Boyer R (1994) *Materials properties handbook: Titanium alloys*. ASM International
23. Ríos S, Colegrove PA, Martina F, Williams SW (2018) Analytical process model for wire + arc additive manufacturing. *Addit Manuf* 21:651–657. <https://doi.org/10.1016/j.addma.2018.04.003>

Publisher's Note Springer Nature remains neutral with regard to jurisdictional claims in published maps and institutional affiliations.